Super-Resolution-Aided Sea Ice Concentration Estimation From AMSR2 Images by Encoder–Decoder Networks With Atrous Convolution

Tiantian Feng, Xiaomin Liu, and Rongxing Li, *Senior Member, IEEE*

***Abstract*—Passive microwave data is an important data source for the continuous monitoring of Arctic-wide sea ice concentration (SIC). However, its coarse spatial resolution leads to blurring effects at the ice-water divides, resulting in the great challenges of fine-scale and accurate SIC estimation, especially for regions with low SIC. Besides, the SIC derived by operational algorithms using high-frequency passive microwave observations has great uncertainties in open water or marginal ice zones due to atmospheric effects. In this article, a novel framework is proposed to achieve accurately SIC estimation with improved spatial details from original low-resolution Advanced Microwave Scanning Radiometer 2 (AMSR2) images, with joint the super-resolution (SR) and SIC estimation network. Based on the SR network, the spatial resolution of original AMSR2 images can be improved by four times, benefiting to construct AMSR2 SR features with more high-frequency information for SIC estimation. The SIC network with an encoder–decoder structure and atrous convolution, is employed to accurately perform the SIC retrieval by considering the characteristics of passive microwave images in the Arctic sea ice region. Experimental results show that the proposed SR-Aided SIC estimation approach can generate accurate SIC with more detailed sea ice textures and much sharper sea ice edges. With respect to MODIS SIC products distributed in Arctic scale, the proposed model achieves a root-mean-square error (RMSE) of 5.94% and mean absolute error (MAE) of 3.04%, whereas the Arctic Radiation and Turbulence Interaction Study (ARTIST) Sea Ice (ASI) SIC results have three and two times greater values of RMSE and MAE.**

***Index Terms*—Arctic sea ice concentration, convolutional neural networks, passive microwave image, super resolution.**

I. Introduction

POLAR sea ice is one of critical parameters of cryosphere and polar environment changes. Over the past several decades, numerous studies show that Arctic sea ice has been undergoing major rapid changes, such as smaller in area and thinner in thickness [1], [2], which is altering global weather conditions and climate. As one of the important physical parameters of sea ice, sea ice concentration (SIC) describes the percentage of sea ice per unit ocean area, intuitively reflecting the amount of sea ice, and can be used for the estimation of other important sea ice parameters (e.g., sea ice area) as well as some representative sea ice features (e.g., polynyas and leads) [3].

The on-site observation of SIC is limited by the harsh geographical environment of the polar regions, while SIC derived from remote sensing observations, especially the passive microwave data, has the potential to achieve Arctic-wide dynamic monitoring of Arctic sea ice [4]. Since the 1970s, satellite passive microwave sensors have been making near-complete daily observations of Arctic sea ice, with the advantages of all-weather operation, wide coverage and high temporal resolution, served as an important data source for Arctic sea ice research and ship navigation [5].

Among representative passive microwave data, the Advanced Microwave Scanning Radiometer 2 (AMSR2) data at the 89-GHz channels have the densest sampling interval, 5 × 5 km, with approximately 3 × 5 km in the footprint size [6]. However, compared with optical and synthetic aperture radar (SAR) images, the relatively coarse spatial resolution results in blurred SIC products, especially at the ice-water divides, leading to great challenges in identifying detailed sea ice features based on SIC maps. For example, it shows that the high-resolution (HR) AMSR2 SIC products with a grid resolution of 3.125 km can provide more details of lead structures than AMSR2 SIC data at lower spatial resolution with a grid resolution of 12.5 km during the February 2013 Fracture Event in the Beaufort Sea [7]. But there are still some narrow leads that cannot be identified by 3.125-km resolution AMSR2 SIC products with limited spatial details, compared with 250-m resolution moderate resolution imaging spectroradiometer (MODIS) images. Moreover, there is a model study of the atmosphere-ocean heat exchange caused by the opening of leads, showing that a 1% of the lead area fraction can change the near-surface air temperature by approximately 3.5 K [8]. Besides, coarse SIC can significantly affect or even endanger human activities, such as the safety of the Arctic ship navigation [9]. Therefore, improving the

Manuscript received 3 September 2022; revised 19 October 2022; accepted 14 December 2022. Date of publication 27 December 2022; date of current version 9 January 2023. This work was supported in part by the National Key Research and Development Program of China under Grant 2017YFA0603100 and Grant 2021YFB3900105 and in part by the National Science Foundation of China under Grant 41801335 and Grant 41941006. *(Corresponding author: Xiaomin Liu.)*

The authors are with the Center for Spatial Information Science and Sustainable Development Applications, College of Surveying and Geo-Informatics, Tongji University, Shanghai 200092, China (e-mail: fengtiantian@tongji.edu.cn; 1811039@tongji.edu.cn; ronli_282@hotmail.com).

Digital Object Identifier 10.1109/JSTARS.2022.3232533

TABLE I
FOOTPRINT SIZES AND SAMPLING INTERVALS OF AMSR2 DATA AT DIFFERENT FREQUENCIES

Frequency (GHz)	6.925	7.3	10.65	18.7	23.8	36.5	89
Footprint (km)	35 × 62	35 × 62	24 × 42	14 × 22	11 × 19	7 × 12	3 × 5
Sampling Interval (km)	10 × 10	10 × 10	10 × 10	10 × 10	10 × 10	10 × 10	5 × 5

spatial resolution of passive microwave images is essential for SIC estimation with improved spatial details, and can benefit to researches on the evolution of Arctic sea ice and fine-scale applications.

Image super-resolution (SR) is a technique widely used in various fields, including passive microwave remote sensing, which reconstructs a HR image with improved spatial resolution from a low-resolution (LR) image or a LR image sequence, making the blurry images more clear and sharper [10]. SR methods proposed for applications in passive microwave images can be divided into two categories: analytical SR methods and deep learning (DL) based SR methods. Analytical SR methods including the Backus–Gilbert (BG) method [11] and reconstruction method [12], are developed using overlapping redundant observations of brightness temperature (T_B) based on the antenna pattern of the passive microwave radiometer. They have managed to improve the spatial resolution of passive microwave images by two to four times, but their performance is limited by the reasonableness of the radiometer antenna pattern assumptions. In contrast, DL-based SR methods can adaptively learn the degradation relationship between HR image and LR image pairs in an end-to-end way without any prior knowledge or assumptions. For example, Hu et al. [13] proposed a single-image SR model based on image degradation and residual network to enhance the spatial resolution with one passive microwave image as input. To make full use of the complementary information between multitemporal LR images, Liu et al. [14] developed a multi-image super-resolution (MISR) network to improve the spatial resolution of sea ice passive microwave images, which is designed according to the characteristics of both passive microwave images and Arctic sea ice scenes. Take SIC estimation as an example, it is shown that finer texture features and sharper sea ice edges are provided on the super-resolved passive microwave images, which is beneficial for fine-scale SIC estimation. However, it remains to be explored whether to further perform supersolved SIC estimation from original LR passive microwave images with a joint SR and SIC estimation network.

According to the different microwave emissivity between sea ice and sea water at different frequencies and different polarization modes, many SIC estimation algorithms based on passive microwave dada have been developed. For example, for the widely used and representative AMSR2 data, the Bootstrap (BT) [15], [16] and the Arctic Radiation and Turbulence Interaction Study Sea Ice (ASI) algorithms [17] are developed as operational SIC estimation algorithms by the Japan Aerospace Exploration Agency (JAXA) and University of Bremen, respectively. The BT algorithm uses low-frequency T_B of AMSR2 at 19-GHz and 37-GHz to estimate SIC, providing available SIC products with the spatial resolution of 10 km or 25 km. And the ASI algorithm performs SIC estimation from the high-frequency AMSR2 data at 89-GHz, and can provide available SIC products with the highest spatial resolution at present, 3.125 km or 6.25 km, thanks to using the smaller footprint and denser sampling intervals of 89-GHz channels than other channels (as shown in Table I) as input. Despite great advantages in resolution, the accuracy of ASI algorithm is reduced due to the atmospheric effects at 89 GHz, such as water vapor and liquid water path, especially for regions with low SIC [17]. There are some weather filters based on the gradient ratio of lower frequencies data, which may filter out not only spurious ice in the open water area but also low concentration sea ice near the ice edge by the given threshold [18]. Therefore, the ASI algorithm has some limitations in the marginal ice zones where thin ice tends to be underestimated, and in open water area where spurious ice may not be removed completely, which are exactly focus areas for operational ice mapping and shipping navigation.

On the other hand, machine learning techniques including DL are widely used in the progress of SIC estimation models from various remote sensing data, and most achieve better performance than above traditional algorithms, such as the BT and ASI algorithms. For example, Chi et al. [19] proposed a multilayer perceptron (MLP) based model to retrieve Arctic SIC, using AMSR2 T_B product at a 10 km spatial resolution as input and down sampled MODIS-derived SIC product as label. The MLP-based model can well describe regions of low-SIC and melting ice in summer. Han et al. [20] developed a random forest (RF) regression model to estimate summer SIC of the Pacific Arctic Ocean, with both AMSR2 T_B product with a grid spacing of 10 km and European Reanalysis Agency-5 reanalysis fields as input. And it can accurately estimate SIC under various atmospheric and ice surface melting conditions. The performance of the above MLP-based model and RF model for SIC estimate generally outperform that of both BT and ASI algorithms. Karvonen [21] adopted MLP model for SIC estimation of the Baltic Sea in winter using the combination of Sentinel-1 SAR and AMSR2 features as input, showing better performance than ASI algorithm.

As the most common DL architecture used in remote sensing, convolutional neural network (CNN) can capture complex nonlinear relationships and achieve very good performances for many cryosphere tasks including SIC estimation, by considering the spatial dependencies between adjacent cells. For example, Wang et al. [22] applied a simple CNN with two pairs of convolution layers and pooling layers with one fully connected layer, to estimate SIC from RADARSAT-2 dual-polarimetric

SAR during the ice melting season. And DenseNet is utilized to predict SIC from RADARSAT-2 SAR image by Cooke and Scott [23], suggesting that CNN is accurate and robust to be used for operational SIC tasks. Limited by the network structure using CNN with fully connected layers at the output, the abovementioned two methods are sensitive to patch size and cannot achieve end-to-end SIC estimate at the pixel level. With an improvement over the previous work, the U-net [24] architecture lacking fully connected layers is a fully convolutional network (FCN) with the encoder–decoder structure, which is applied in many newly published works for SIC estimation from SAR images [5], [6], [25]. Considering the advantages of SAR images with high spatial resolution and AMSR2 data with the independent of the wind conditions, a CNN architecture with atrous spatial pyramid pooling (ASPP) is designed for fusing Sentinel-1 SAR imagery and AMSR2 data with large resolution differences [26], inspired by the more advanced FCN architectures named Deeplab [27]. Combining SAR and passive microwave data that they have short time lag, the spatial resolution of SIC can be higher than that of using passive microwave data alone, but limited by the availability of SAR data as well as additional data uncertainties from different sources. Besides, SAR images have difficulty in achieving Arctic-wide dynamic monitoring due to its low temporal resolution, whereas passive microwave data have the potential to provide high spatial-temporal observations for Arctic sea ice, with the advantage of its high temporal resolution as well as the possibility of improved spatial resolution by SR technology. Therefore, CNN-based methods for SIC estimation from passive microwave data should be further explored to obtain more accurate Arctic SIC products.

In this article, we propose a novel framework with joint SR and SIC estimation network to achieve accurate SIC estimation with improved spatial details from original LR AMSR2 passive microwave images, where the SR network can successfully improve the spatial resolution of original Arctic sea ice passive microwave images and the following SIC estimation network can accurately perform the retrieval of Arctic SIC. The proposed framework can reduce the uncertainties of SIC estimation, resulting from the coarse spatial resolution of original AMSR2 images and inaccuracy estimation due to limitations of the traditional retrieval algorithms, especially for low SIC regions. In addition, to illustrate the performance and effectiveness of the proposed framework, some quantitative comparisons and visual comparisons between SIC estimated by ASI algorithm and that of proposed method are achieved.

The main contributions of this article can be summarized as follows.

1) A novel framework with joint SR and SIC estimation network is proposed to accurately perform fine-scale SIC estimation from original LR AMSR2 passive microwave images. The proposed method is present to outperform other state-of-the-art SIC estimation algorithm (i.e., ASI algorithm).
2) To reduce the blurring effects at the ice-water divide and the errors of SIC estimation caused by coarse spatial resolution, the advanced SR network (PMDRnet) is applied to improve the spatial resolution of original LR AMSR2 images.
3) To accurately estimate SIC and consider the characteristics of passive microwave images in the Arctic sea ice region, the efficient CNN-based network with an encoder–decoder structure and atrous convolution is adopted as the SIC network, showing good robustness in different regions at different times of the Arctic.

The rest of this article is organized as follows. Data used in this article are briefly described in Section II and Method is presented in Section III. Section IV shows the experimental results and discussions. Finally, Section V concludes this article.

II. Data

A. AMSR2 Data

AMSR2 is equipped on the Global Change Observation Mission 1st - Water "SHIZUKU" (GCOM-W1) satellite [28]. It enables the global estimation of a variety of geophysical parameters with a higher spatial resolution, such as SIC and sea surface temperatures. AMSR2 takes measurements at seven frequencies and two polarizations (horizontal (H) and vertical (V) polarization), whose footprint sizes and sampling intervals are shown in Table I.

In this article, AMSR2 level 1B T_B swath data at 89-GHz dual-polarized channels, provided by JAXA, are employed because of the highest spatial resolution and available sea ice information. For better data preprocessing and feature extraction, all the AMSR2 swath data for each day are gridded into polar stereographic grids of the National Snow and Ice Data Center (NSIDC) [29] using nearest Gaussian weighting,[1] respectively. And the grid resolution of 6.25 km is chosen, which is a tradeoff between generating embedded HR images and reducing errors during the gridding process [14]. Both gridded AMSR2 images with H and V polarization are 16-bit gray images, whose values are the original T_B multiplied by the scale factor of 100. Nan values are in the gridded AMSR2 images are replaced with 30 000. The extent of the gridded daily AMSR2 image is drawn in Fig. 1, including the entire Arctic, with a size of 760×890 pixels. Each image is clipped into small patches of size 128×128 pixels in an overlapping manner. The image acquisition time range is from 2020 to 2021, and images with missing or incorrect information or no corresponding label image are discarded.

B. MODIS SIC Products

MODIS SIC products, released by the University of Bremen are used as labels when training the SIC network and reference data for evaluation of the proposed framework. The data are provided daily since 2017 and are only available between October 1st and May 31st. The thermal infrared spectrum data of MODIS onboard NASA's Aqua satellites are employed to derive the MODIS SIC products, which have a higher spatial resolution of 1 km and are available over the entire Arctic region in cloud-free conditions. In addition, The Aqua satellite

[1] [Online]. Available: https://pyresample.readthedocs.io/en/latest/swath.html

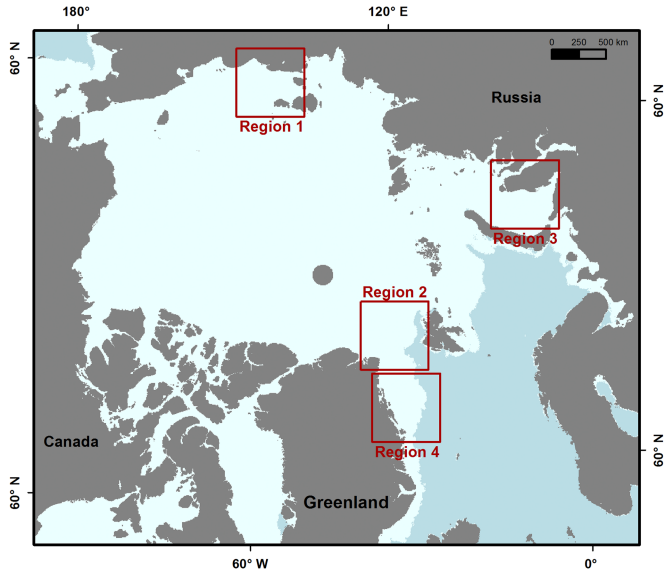

Fig. 1. Areas of AMSR2 data used in the study. The gray area is land mask and missing data; the blue area is sea water; and the light blue area is sea ice where SIC is above 15% on February 1, 2020, downloaded from the University of Bremen at https://seaice.uni-bremen.de. The red rectangular regions 1, 2, 3, and 4 are selected for visual comparisons.

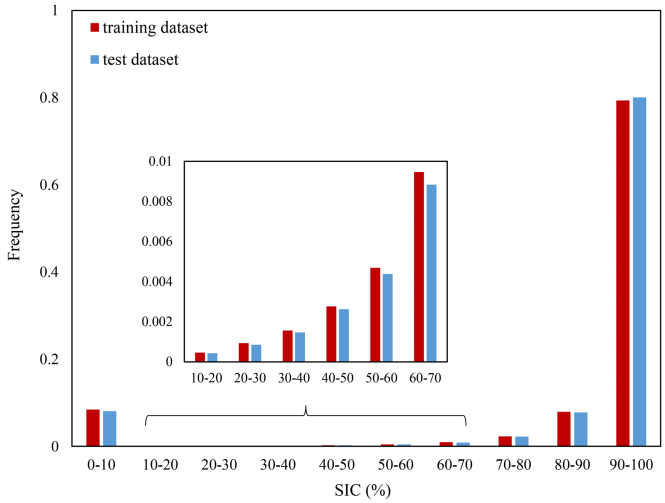

Fig. 2. SIC distribution of the training and test datasets. Zoomed-in view in the middle of the graph shows the SIC intervals between 10% and 70%.

has similar orbit characteristics to GCOM-W1 and flies 4 min behind GCOM-W1, resulting in the short time lag (normally between 3 and 8 min) between MODIS Aqua and AMSR2 [19]. The MODIS SIC products are determined based on the local temperature anomaly using the algorithm presented in Ludwig et al. [3].

The temporal and spatial coverage of MODIS SIC products used in this article are consistent with AMSR2 images. The data are resampled to the NSIDC grid with grid spacing of 1.5625 km (4 times the AMSR2 images) by using bicubic interpolation for comparison with the estimated SIC of the network, with a size of 3040×3560 pixels. Multiple smaller patches from each image are created by cropping in the same manner as AMSR2, 512×512 pixels in size, with the same spatial extent as the corresponding AMSR2 samples, but with 4 times the grid resolution.

C. Dataset Distribution

The training and the test datasets are randomly selected among the 11968 image/label sample pairs at a ratio of approximately 9 to 1, of which 10 772 for training and 1196 for test. The samples are spatially well distributed over the sea ice covered areas of the Arctic, with about the same number of samples per month. The frequency distribution of the training and test datasets is shown in Fig. 2, which is divided into 10 statistical intervals according to the SIC distribution characteristics. The frequency distributions of training and test datasets are similar in each interval, but they both have the problem of unbalanced distribution, i.e., the number of pixels in the medium SIC values are very small compared with that of high SIC values, especially for SIC intervals between 10% and 70%, which is presented as the zoomed-in view in the middle of the Fig. 2. It is worth noting that unbalanced distribution of training dataset will push the model to pay more attention to represented SIC values and less to the underrepresented SIC values, resulting in poor performance of model.

III. Methods

The pipeline of the proposed framework is present in Fig. 3, which consists of two main components, SR network and SIC network. In order to obtain fine SIC results, the AMSR2 LR image sequence $\{I_{t-2}^{\mathrm{LR}}, I_{t-1}^{\mathrm{LR}}, I_t^{\mathrm{LR}}, I_{t+1}^{\mathrm{LR}}, I_{t+2}^{\mathrm{LR}}\}$ is first input into the pretrained SR network, and then AMSR2 SR features including the super-resolved AMSR2 images I_t^{SR} and constructed multichannel features of sea ice P_t^{SR} with the improved spatial resolution are as the input of the SIC network together with the corresponding labels for model training, which will output the estimated SIC during test phase.

A. SR Network

In the SR component of the framework, we adopt a MISR network called PMDRnet, which is designed to improve the spatial resolution of sea ice passive microwave images [14]. Similar to other general DL-MISR algorithms, PMDRnet includes four processes: feature extraction, feature alignment, adaptive fusion, and SR reconstruction, as shown at the top of Fig. 3. With the novel progressive alignment strategy and multiscale deformable convolution alignment unit in the feature alignment module, the PMDRnet can handle complex and large Arctic sea ice motions even with large geometric changes to achieve good alignment performance. And it can adaptively fuse the effective spatiotemporal information across sequence for remaining unaligned features and occlusion problems by the temporal attention mechanism in the adaptive fusion module. Besides, the sea ice related loss function is designed based on the polarization difference of the T_B at multichannel AMSR2 images, so as to improve SR performance and achieve better estimation results of Arctic SIC. With the pretrained PMDRnet, the

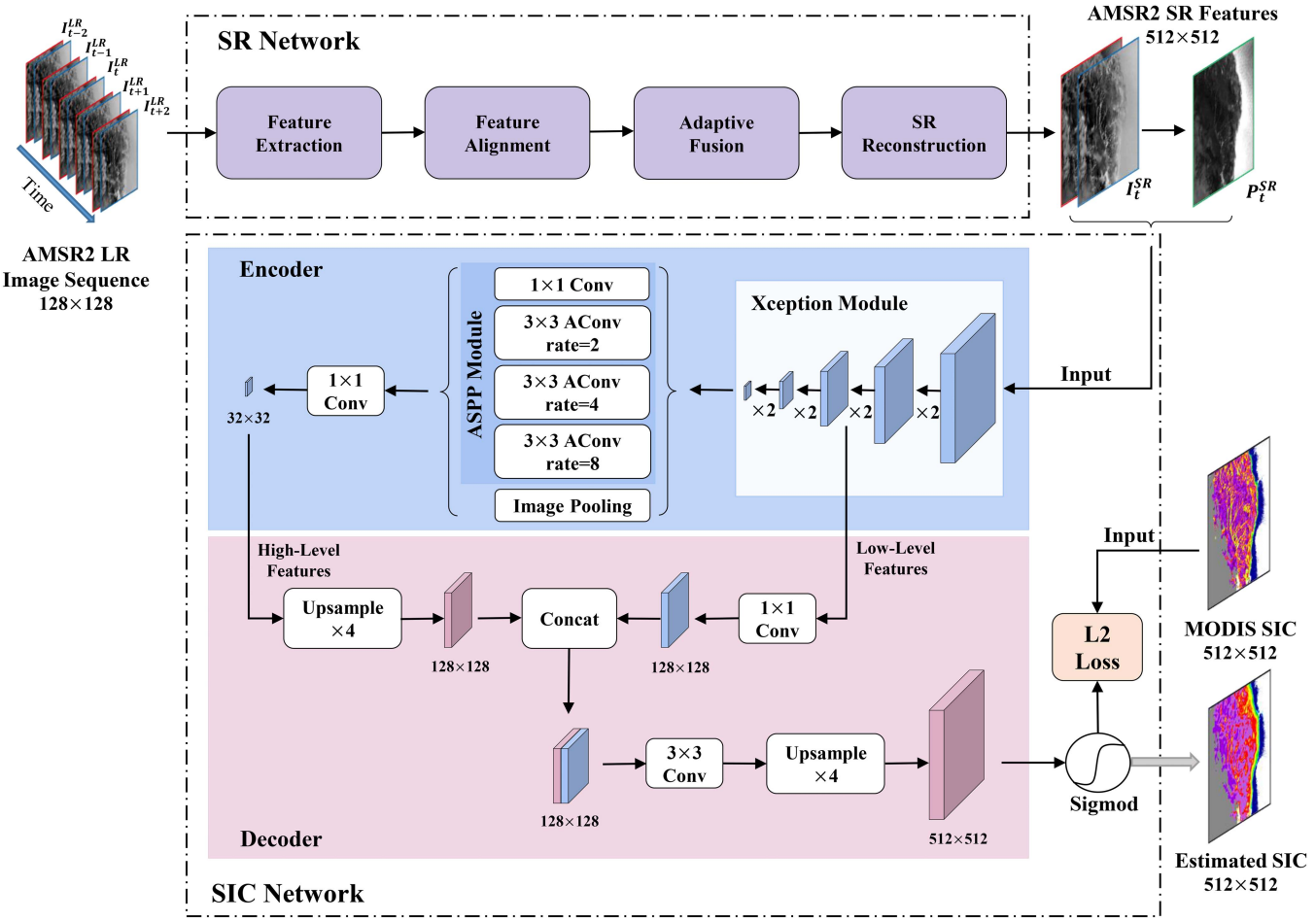

Fig. 3. Pipeline of the proposed framework, where the top is SR network and the bottom is SIC network. For SR network, the input is AMSR2 LR images sequence consisting of five neighborhood images $\{I_{t-2}^{\mathrm{LR}}, I_{t-1}^{\mathrm{LR}}, I_t^{\mathrm{LR}}, I_{t+1}^{\mathrm{LR}}, I_{t+2}^{\mathrm{LR}}\}$, and the middle image I_t^{LR} is the target image to be super-resolved. The input and output of the network are dual-channel data, including the H polarization images (images with red borders) and V polarization images (images with blue borders) at 89-GHz channels. The output SR image I_t^{SR} and the polarization difference P_t^{SR} (image with green border) are served as the inputs of following SIC network. MODIS SIC products is utilized as the label in the training phase. In the test phase, the output estimation is denoted as the solid gray arrow. The "Conv," "AConv," and "Concat" in the figure denote the convolution, atrous convolution, and concatenation operation, respectively.

spatial resolution of original Arctic sea ice passive microwave images can be successfully improved by four times, from 6.25 to 1.5625 km, and it is proved that the SR performance of PMDRnet is very good. For instance, based on simulated AMSR2 data, PMDRnet significantly outperforms current state-of-the-art MISR methods, where performance is evaluated quantitatively via the peak signal-to-noise ratio and the structural similarity index. In addition, for the application of actual AMSR2 data, SIC oriented from SR results generated by PMDRnet is calculated using ASI algorithm [17] and compared to SIC oriented from MODIS images, which achieves a good performance in terms of qualitative and quantitative comparisons. Therefore, PMDRnet is a very suitable approach to ensure the acquisition of reliable sea ice AMSR2 SR features served as input of following SIC network.

B. SIC Network

When designing or applying the network for SIC estimation, it is necessary to consider the characteristics of passive microwave images in the Arctic sea ice region. First, the spatial resolution of passive microwave images is much lower compared to natural images (RGB images), resulting in the lack of sufficient high-frequency information, which makes extraction of sea ice features more difficult. Second, there are sea ice features at different scales in the Arctic, including ice floes, openings in the sea ice, and sea ice edges at different sizes. Third, sea ice features are difficult to be inversed from single-channel passive microwave images due to the insufficient sea ice information, which requires the combination of multichannel passive microwave images as input data.

The CNN model chosen for the SIC estimation is inspired by Deeplabv3+ [30], which achieves a new state-of-art performance on the PASCAL VOC 2012 semantic segmentation benchmark. As shown at the bottom of Fig. 3, the encoder–decoder structure is employed in the SIC network, where the encoder module gradually reduces the feature maps to captures higher semantic information and the decoder module gradually recovers the spatial information to obtain sharper boundaries of sea ice. The modified Xception module in [30] is used as network

backbone for the feature extraction, which is deeper and uses depthwise separable convolution with striding to replace the max pooling operations, achieving better performances with faster computation. Following the output features of backbone that are 16 times smaller than input resolution by $\times 2$ downsampling four times, ASPP module consisting of several parallel atrous convolution with different rates, is used to increase the field-of-view of filters to capture rich multiscale information. The output features from ASPP module as well as the added image-level features are integrated together as the encoder output features via the concatenation operation and a 1×1 convolution layer, which contains 256 channels and rich semantic information. For the decoder part, 256 high-level features generated by the encoder are directly upsampled by 4 times and concatenated with the 48 low-level features from the network backbone by 1×1 convolution, where they have the same spatial resolution. Finally, a 3×3 convolution and upsampling operation by four time are performed to obtain pixel-level estimated SIC.

There are some modifications made to Deeplabv3+ model when applying to this article. First, the network input is AMSR2 SR images and constructed multichannel features instead of RGB images, including AMSR2 SR images at 89-GHz dual-polarized channels I_t^{SR} as well as their polarization difference P_t^{SR} by subtracting from V polarization to H polarization, where constructing multichannel features of sea ice is beneficial to enhance the sea ice information in the network. The SIC estimation can be formulated as a regression problem for directly estimating SIC, or a classification problem for predicting discrete categorized SIC [26]. In this article, the SIC estimation is modeled as a regression problem. However, the original Deeplabv3+ is designed for image semantic segmentation or classification, and needs to be modified for SIC regression. The final *softmax* classification layer in Deeplabv3+ is removed, replaced with a nonlinear activation function *sigmoid*. And the output of SIC network in the range [0, 1] is directly as an SIC estimation, where 1 indicates pure ice and 0 open water.

C. Weighted Loss Function

In terms of training the SIC network to estimate SIC value, one of the most widely used loss functions in regression problems, the L2 loss functions, is used. It is used to minimize the errors calculated by averaging the square of the difference between the reference SIC and the output SIC estimated by the model. Considering unbalanced frequency distribution of training dataset mentioned in Section II, the weighted L2 loss function is used to increase the modeling capability of the network for the SIC values with a small number of pixels. The weight is defined as (1), which is negatively correlated with the frequency of the ith SIC category

$$W_i = \frac{\sum_{i=1}^{n} \log_{10} N_i}{n * \log_{10} N_i} \tag{1}$$

where n is the total number of SIC categories with the value of 10, which is consistent with the statistical intervals of SIC shown in Fig. 2. W_i is the SIC weight of pixels belonging to the ith SIC category, and N_i is the total number of pixels of ith SIC category. Based on the data distribution of training dataset, the weights of all the SIC intervals are as follows:

$$W_{12,\cdots,10} = [0.8833, 1.2355, 1.1722, 1.1304, 1.0866, 1.0493, 1.00035,\ 0.9509,\ 0.8863,\ 0.7868]$$

In addition, the weights of masked pixels are defined as 0, including land or no data pixels, which will be ignored in training phase. The weighted L2 loss function for across all the pixels in a batch is defined as

$$\text{loss} = \frac{\sum_{j=1}^{N_{\text{pixels}}} W_i * (y_j - \tilde{y}_j)^2}{N_{\text{pixels}}}. \tag{2}$$

For the jth pixel belonging to the ith SIC category, y_j is the true SIC provided to the network, and $\tilde{y}_j$ is the estimated SIC of the network. N_{pixels} is the number of all pixels in a batch.

IV. Results and Discussions

In this section, for the experimental evaluation of the performance of the proposed framework including SR network and SIC network, the SIC estimations are compared with the MODIC SIC products, denoted as MODIS SIC, in terms of quantitative comparison and visual comparison. In addition, an ablation study is performed to verify the effectiveness of SR network and SIC network, and SIC estimation from original LR AMSR2 images using ASI algorithm (LR-ASI SIC) is selected as the baseline, which is compared with that of SR-ASI method (the SIC estimation method in [14]) by using the SR AMSR2 images instead of LR AMSR2 images used in LR-ASI method. And SR-DL model further replaces ASI method with the SIC network to perform SIC estimation (SR-DL SIC) based on SR-ASI method.

A. Parameter Settings

The hyper-parameters of SR network are the same as PMDR-net [14]. As for SIC network, the Xception module employs 20 residual blocks for feature extraction, consisting of three 3×3 depthwise separable convolutional layers, each followed by a batch normalization and the rectified linear unit activation function. For the first three residual blocks, the number of filters in each layer is, respectively, 128, 256, 728, and the stride of each layer of each residual block is 1 except the last layer is 2. Following by 16 residual blocks, the number of filters in each layer is 728, and the stride is set as 1 for each layer. The last block consists of a layer with 728 filters and stride $= 1$, one with 1024 filters and stride $= 1$, and one with 1024 filters and stride $= 2$. The dilation rates of the atrous convolutional layer in the ASPP module are set with the value of 2, 4, 8, where the model has the best performance for AMSR2 passive microwave data and sea ice scenes during the experiments. The AMSR2 input data of the network need to be normalized in the range of $[-1, 1]$ using min-max normalization method with the minimum value is 10 000 and maximum value 30 000, for which improves the convergence speed when training model. The SIC value in percentage is divided by 100 to make its data range [0, 1], which is consistent with the range of function *sigmoid*. The input data

of network include 512×512×3 AMSR2 image features, and 512×512×1 MODIS SIC labels.

The proposed network is implemented on the Tensorflow framework (version 1.15) in a Python (version 3.7) environment and trained using 2 NVIDIA GTX2080Ti GPUs. The parameters of the network are optimized using the momentum optimizer with $\beta = 0.9$, and the learning rate is set to 5×10^{-4}.

B. Training/Test Procedure

The optimal parameters of SR network are from the final pretrained PMDRnet model with the best performance, which are trained utilizing a large external AMSR2 HR/LR image pairs dataset. Because the distribution of data samples in this article is the same as that of PMDRnet, with few differences in time and space distributions, the previous parameters are used without retraining the SR network. The corresponding relationship between degrading LR images and HR images in the training dataset is expressed in the whole model parameters, including extracting representative sea ice features from the input LR images, accurately aligning neighborhood images to the target image to be super-resolved, providing effective information for the target image during fusion, and finally reconstructing the SR image with high frequency information. To obtain SR image output served as the input of SIC network, each LR patch sequence $\{I_{t-2}^{\mathrm{LR}}, I_{t-1}^{\mathrm{LR}}, I_t^{\mathrm{LR}}, I_{t+1}^{\mathrm{LR}}, I_{t+2}^{\mathrm{LR}}\}$ with the grid resolution of 6.25 km is input into the pretrained SR network to obtain the corresponding SR patch I_t^{SR} with the grid resolution of 1.5625 km, all of which are AMSR2 data at 89-GHz dual-polarized channels, as shown in Fig. 3.

In contrast, the parameters of the layers except for the last layer in SIC network are initialized with the Deeplabv3+ model parameters pretrained with the ImageNet data and PASCAL augmented training set [30], and then the learned parameters are transferred to the domain of AMSR2 passive microwave images. For the last layer, the initial parameters are randomly initialized within the range of [0, 1]. The super-resolved 1.5625-km AMSR2 data at 89-GHz dual-polarized channels I_t^{SR} and their polarization difference P_t^{SR} are used as input for the training, while the downsampled 1.5625-km MODIS SIC products are used as the labels. Random scale data enhancement is used in the training process. When trained to be optimal, the parameters of the final network are perfectly fine-tuned to SIC regressive task using AMSR2 passive microwave images. In the testing phase, the AMSR2 SR data over the target region to be estimated for SIC is taken as input, and the estimated SIC is obtained through the inference process of the trained SIC network.

C. Evaluation Criterion

For the evaluation of model performances, four difference criterions are employed to make the measurements, including root-mean-square error (RMSE), mean absolute error (MAE), mean bias (MBIAS), and standard deviation of bias (STD), which is defined as

$$\mathrm{RMSE} = \sqrt{\frac{\sum_{k=1}^{M} e_k^2}{M}} \tag{3}$$

TABLE II
RESULTS OF EXPERIMENTAL EVALUATION AND ABLATION STUDY. RMSE, MAE, MBIAS, AND STD FOR THE TEST DATASET BETWEEN MODIS SIC AND SIC ESTIMATIONS FROM LR-ASI, SR-ASI, AND SR-DL, RESPECTIVELY

Model	LR-ASI	SR-ASI [14]	SR-DL (Ours)
SR network	×(LR)	√	√
SIC network	×(ASI)	×(ASI)	√
RMSE	16.74%	12.42%	5.94%
MAE	7.27%	5.36%	3.04%
MBIAS	0.31%	2.12%	-0.05%
STD	16.74%	12.24%	5.94%

$$\mathrm{MAE} = \frac{\sum_{k=1}^{M} |e_k|}{M} \tag{4}$$

$$\mathrm{MBIAS} = \frac{\sum_{k=1}^{M} e_k}{M} \tag{5}$$

$$\mathrm{STD} = \sqrt{\frac{\sum_{k=1}^{M} (e_k - \mathrm{MBIAS})^2}{M}} \tag{6}$$

where M is the number of pixels over the whole area to be estimated, e_k is bias between the estimated SIC $\tilde{y}_k$, and the true SIC y_k for the k th pixel.

D. SIC Estimation

1) Quantitative Comparison: For all pixels in the test set, distributed in different regions of the Arctic, RMSE, MAE, MBIAS, and STD between MODIS SIC and LR-ASI SIC, SR-ASI SIC, and SR-DL SIC are calculated, as shown in Table II, respectively. By comparing the results of LR-ASI SIC and SR-ASI SIC, which are all calculated using ASI algorithm, it is evident that the error of the SIC estimation from the super-resolved AMSR2 images generated by SR network can be significantly reduced compared with AMSR2 LR images input, especially RMSE decreased by 4.32% and MAE decreased by 1.91%. This shows that the uncertainty of SIC estimation caused by coarse spatial resolution of AMSR2 images can be reduced to some extent with SR network. The comparison results indicate that the MBIAS of SR-ASI is slightly greater in magnitude than that of LR-ASI, but with a smaller STD. In addition, the accuracy of SIC estimation based on SIC network is further improved. Compared with the evaluation results of SR-ASI, RMSE of SR-DL decreases from 12.42% to 5.94%, MAE from 5.36% to 3.04%, MBIAS from 2.12% to -0.05% with the 6.30% decrease of STD. As a result, the results show SR-DL has a significant advantage over LR-ASI in accuracy, and demonstrates the effectiveness of SR network and SIC network.

In order to explore the estimation accuracies of different concentrations at low, medium, and high levels, the SIC is divided into ten categories according to 10% interval, and the average SIC of all pixels for each SIC category is calculated, respectively. The comparisons between the average MODIS SIC and LR-ASI SIC, SR-ASI SIC, or SR-DL SIC in each SIC category are shown in Fig. 4. Compared with LR-ASI SIC, SR-ASI SIC, and SR-DL SIC are more similar to MODIS SIC, with a bias close to the unit

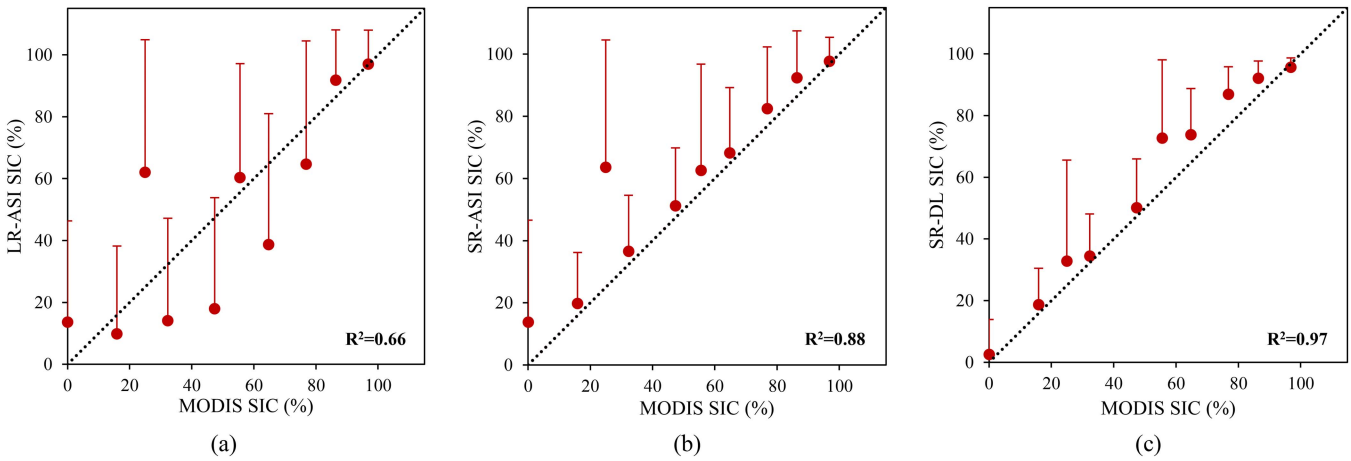

Fig. 4. Comparison for each SIC category between (a) LR-ASI SIC, (b) SR-ASI SIC, (c) SR-DL SIC, and MODIS SIC, respectively. Red dots indicate the comparison between the average MODIS SIC and LR-ASI, SR-ASI, or SR-DL in each ice concentration category. Bars indicate the positive standard deviation, and negative is not shown. The black dotted line represents the unit line.

TABLE III
RMSE, MAE, MBIAS, AND STD FOR DIFFERENT ICE CONCENTRATION CATEGORIES BETWEEN MODIS SIC AND SIC ESTIMATIONS FROM LR-ASI, SR-ASI, OR SR-DL

Evaluation metric	Method	SIC categories according to 10% interval									
		0-10	10-20%	20-30%	30-40%	40-50%	50-60%	60-70%	70-80%	80-90%	90-100%
RMSE (%)	LR-ASI	35.34	29.03	56.85	37.30	46.78	37.12	49.05	42.78	16.98	10.98
	SR-ASI	35.50	16.96	56.47	17.94	19.27	34.92	20.99	20.64	16.13	7.90
	SR-DL	11.59	12.19	33.56	13.69	16.16	30.45	16.90	13.93	8.17	3.45
MAE (%)	LR-ASI	13.63	22.06	51.60	35.54	46.08	33.63	44.21	33.00	12.70	4.42
	SR-ASI	13.75	4.21	50.21	6.06	8.32	31.37	13.17	15.36	12.40	3.73
	SR-DL	2.52	3.37	28.24	5.19	7.43	27.98	11.27	11.30	6.71	2.26
MBIAS (%)	LR-ASI	13.60	-6.06	37.04	-18.21	-29.39	4.77	-26.07	-12.21	5.44	0.19
	SR-ASI	13.73	3.86	38.66	4.24	3.87	7.02	3.47	5.66	6.05	0.89
	SR-DL	2.49	2.75	7.84	2.18	2.71	17.12	9.02	10.01	5.69	-1.24
STD (%)	LR-ASI	32.62	28.39	43.13	32.55	36.39	36.82	41.55	41.01	16.09	10.98
	SR-ASI	32.74	16.52	41.18	17.43	18.88	34.21	20.70	19.85	14.95	7.84
	SR-DL	11.32	11.87	32.63	13.52	15.93	25.18	14.29	9.68	5.86	3.22

line. For the statistical R^2 coefficient measuring the similarity between two sets of SIC values, SR-DL SIC has the highest R^2-score, with the value of 0.97, showing good consistency with MODIS SIC in different SIC categories. For example, it is quite clear that SR-DL has significantly smaller bias than LR-ASI and SR-ASI for the 20–30% SIC category. Additionally, it can be seen that there is a larger negative bias associated with the LR-ASI in 10–20%, 30–40%, 40–50%, 60–70%, and 70–80% SIC category, which will compensate for the positive bias for other ice concentration categories. On the other hand, SR-ASI has positive and small bias for each category, which can explain why the MBIAS of SR-ASI is larger than that of LR-ASI in terms of overall evaluation in Table II. And the biases of SR-DL are similar to that of SR-ASI in 0–90% SIC category, with slightly positive, but it is slightly negative in 90–100% SIC category that nearly 80% of the samples fall into (see Fig. 2), resulting in the slightly negative MBIAS of SR-DL in Table II.

For the pixels belong to low SIC area with open water and very open drift ice, i.e., 0–10% SIC category, both LR-ASI and SR-ASI seem to moderately overestimate SIC values, and SR-ASI has a slightly larger RMSE, MAE, MBIAS, and STD than LR-ASI (see Fig. 4 and Table III), which may be due to the generation of noise accompanied by high frequency information in the SR process. The bias is greatly reduced for SR-DL by using SIC networks, with the smallest MBIAS and STD. Meanwhile, compared with LR-ASI and SR-ASI, RMSE of SR-DL in the low SIC area (i.e., 0–10% SIC category) is reduced by more than 20%, MAE by ∼11%, MBIAS by ∼11%, and STD by ∼21%. These results indicate that ASI algorithm has the problem of mis-estimating in open water area, while SIC network shows good performance for SIC estimation and strong robustness dealing with the noise problem in the SR process. For all three methods, the overall accuracy is higher in the high SIC area (i.e., 80–100% SIC category) compared to other SIC categories, with SR-DL being the best, SR-ASI the second, and LR-ASI the worst in

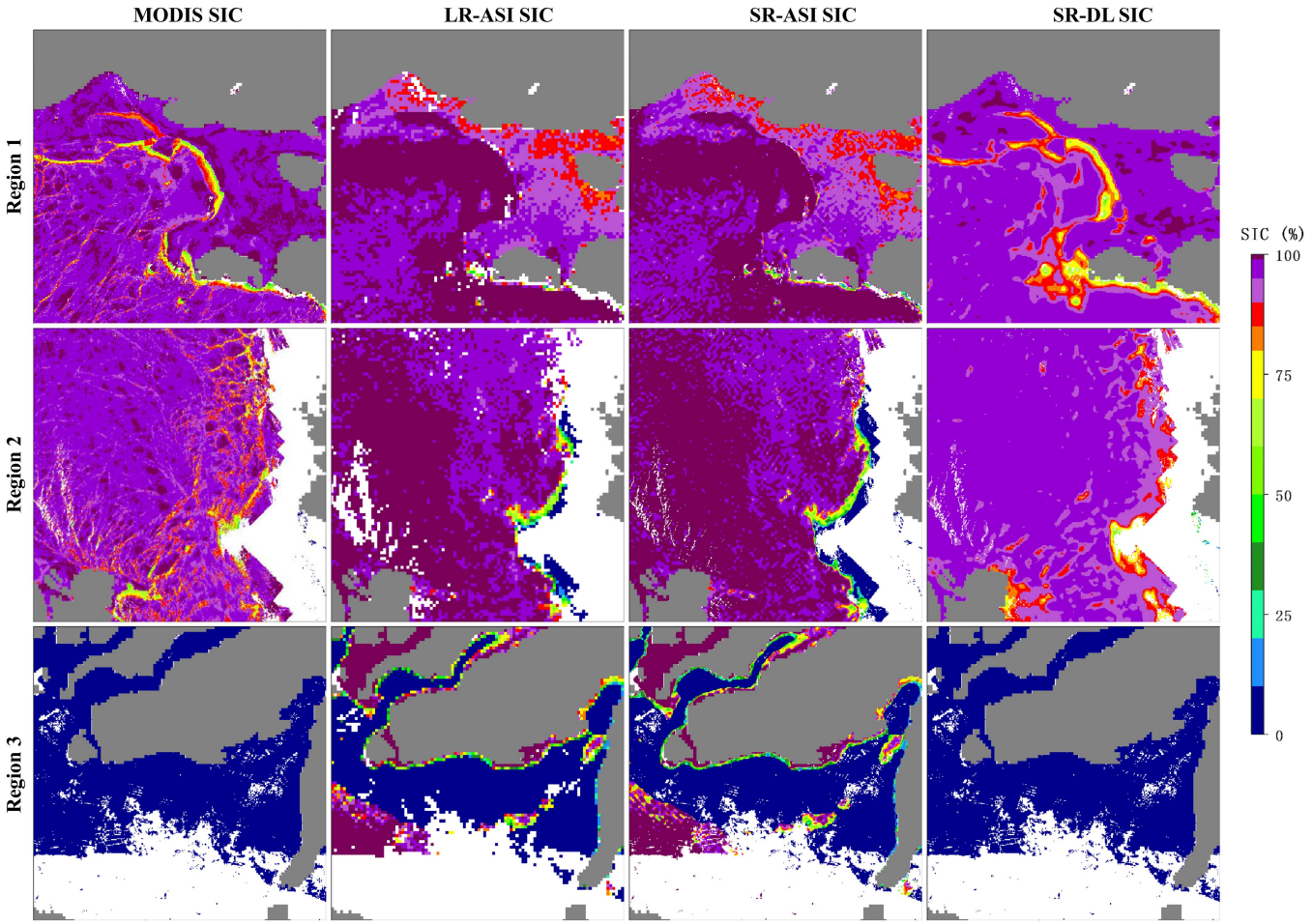

Fig. 5. Comparison for different SIC maps of Region 1, 2, and 3 in Fig. 1, including MODIS SIC, LR-ASI SIC, SR-ASI SIC, and SR-DL SIC (From the left, columns 1 through 4). The dates are March 11, 2020, February 1, 2020 and May 12, 2020 (From top to bottom, rows 1 through 3). The gray area is land mask and the white area is no data on MODIS SIC map.

terms of RMSE, MAE, and STD. And the MBIAS of SR-DL and SR-ASI are slightly larger than LR-ASI in magnitude, especially SR-DL in 90–100% SIC category, due to the tendency of more small errors with consistent signs given the smaller absolute errors. In contrast, the errors are larger in the medium SIC area (i.e., 10–80% SIC category) compared with low and high SIC areas, where it is difficult to perform accuracy SIC estimation using ASI algorithm with limited ability in marginal areas and SIC network with inadequate medium SIC samples and difficult learning tasks. Compared with LR-ASI, RMSE, MAE, and STD of SR-ASI are significantly reduced for 10–80% SIC category, and those of SR-DL are further reduced, which benefit from the powerful capabilities of SR network and SIC network. In addition, the SR-ASI has smaller MBIAS than LR-ASI, except that 20–30% and 50–60% SIC categories overestimate more. And SR-DL has smallest MBIAS in 10–50% SIC category, while largest MBIAS in 50–60% SIC category and moderate MBIAS in 60–80% SIC categories. It indicates that there may be a more systematic bias in a smaller magnitude according to the fact of a larger MBIAS but a smaller MAE, such as SR-DL SIC in 50–80% SIC categories and SR-ASI in 20–30% and 50–60% SIC category, in contrast to LR-ASI, which has more pronounced random bias in a larger magnitude.

In general, the accuracy of SR-DL is better than that of SR-ASI, and LR-ASI is the worst. Second, for the low, medium, and high SIC areas, the error of the three methods is the smallest in the high SIC area, and largest in the medium SIC area. It is concluded that SIC estimation of SIC network outperforms that of ASI algorithm, using SR image better than that using LR image.

2) Quantitative Comparison: To further demonstrate whether the HR sea ice features and patterns on the SIC maps of different methods are reasonable, four regions are selected for visual comparison, whose positions are shown in the red box in Fig. 1. In addition to being limited by the availability of MODIS images, the principles of region selection take different SIC distributions into account, such as low, medium and high SIC regions, and focus on a variety of sea ice characteristics on the SIC maps, such as floating ices and openings in the ice cover in the active sea ice regions, and the boundary between sea ice and land located in relatedly stationary scenes.

MODIS SIC, used as reference, and SIC estimation results from different algorithms in regions 1 to 3 are shown in Fig. 5, mainly low and high SIC areas, which are distributed in East Siberian Sea (see Fig. 1, region 1), Fram Strait (see Fig. 1, region 2), and Kara Sea (see Fig. 1, region 3). For the scene of region

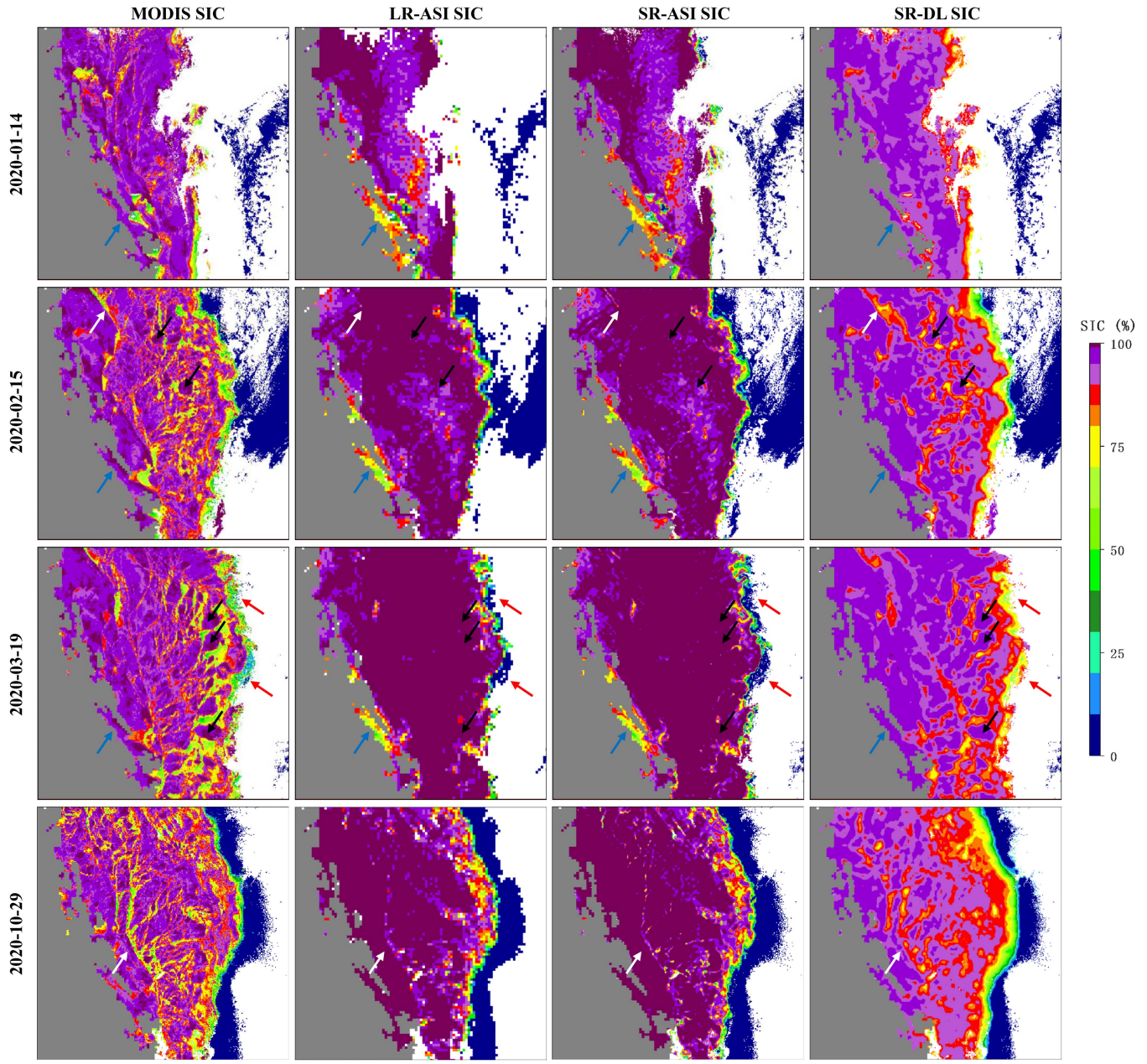

Fig. 6. Comparison for different temporal SIC maps of Region 4 in Fig. 1, including MODIS SIC, LR-ASI SIC, SR-ASI SIC, and SR-DL SIC (From left to right, columns 1 through 4). The dates are January 14, 2020, February 15, 2020, March 19, 2020 and October 29, 2020 (From top to bottom, rows 1 through 4). The gray area is land mask and the white area is no data on MODIS SIC map. Where white, black, blue, and red arrows indicate texture details of sea ice, floating ices, fast ice regions, and marginal ice regions, respectively.

1 with the boundary between sea ice and land in Fig. 5, SR-DL method successfully recover a formed opening in the ice cover and obtained the correct shape and texture details, while LR-ASI and SR-ASI methods fail to resolve the HR features of sea ice due to the limitations of spatial resolution and ASI algorithm. There are few differences between SR-ASI and LR-ASI in general, but SR-ASI has more details. The comparisons in region 2 show that the SR-DL method performs markedly better than LR-ASI and SR-ASI methods, and can capture more high-frequency information of sea ice, whose SIC value is most similar to the MODIS SIC compared to LR-ASI and SR-ASI methods. It is important to note that the LR-ASI and SR-ASI methods misidentify what is clearly sea ice in the MODIS SIC map as sea water, which is correctly estimated in the SR-DL SIC map. The white mask area next to the underestimated region in ASI algorithm is due to the lack of data in MODIS by cloud occlusion, which is actually open water area, where the ice in the marginal ice area tends to be eliminated using the weather filters. Similarly, from the SIC results obtained on the very open water scene of region 3 in Fig. 5, LR-ASI and SR-ASI methods identify open water as sea ice, i.e., spurious ice, which may not be removed cleanly by weather filters. And it is consistent with the previous conclusion in quantitative comparison that ASI methods have a larger error in low SIC areas.

Fig. 6 shows the SIC results of region 4 on Greenland Sea at different times in 2020, belonging to an active sea ice region with lots of floating ices and openings in the ice cover as well as boundaries between sea ice and open water. On the whole, compared with MODIS SIC, SR-ASI SIC has more sea ice features than LR-ASI SIC in all times, providing much sharper sea ice edges and finer texture details, which is important to achieve fine-scale sea ice dynamic monitoring and better navigation guidance. On the other hand, SR-ASI method has some misestimates and the limited ability to perform HR features extraction using ASI algorithm, which cannot be solved by the aid of SR network but needs to depend on the strong regression ability of SIC network. For example, it can be found that there are many medium SIC pixels in the middle of the four temporal MODIS SIC maps with high SIC in Fig. 6, forming many texture details marked by white arrows in the second and fourth row, whose patterns are clearly visible in SR-DL, but not in LR-ASI and SR-ASI SIC maps. In addition, there are many large floating ices in the middle of region 4 on the MODIS SIC map in the second to third row of Fig. 6, shown by black arrows, whose shapes and positions can be basically extracted from the SR-DL SIC map but cannot be identified from the LR-ASI and SR-ASI SIC maps. In the fast ice region of the first to third row indicated by blue arrows, MODIS and SR-DL SIC maps are 90–100% SIC, but LR-ASI and SR-ASI SIC maps 60–80% SIC. And in the third row of Fig. 6, the pixels of marginal ice regions are estimated correctly as 10%–70% SIC by SR-DL method, while the LR-ASI and SR-ASI methods estimate as sea water, which are marked with red arrows. Although the SR-DL method can correctly extract most of sea ice features and patterns, there are still some limitations, such as the overestimation of medium SIC pixels, associated with reduced modeling ability of SR-DL method for the underrepresented SIC values due to insufficient samples. Overall, SR-Aided SIC estimation framework has a good performance at the different region at different times of the Arctic, and can obtain accurate SIC with improved spatial details.

V. Conclusion

In this article, we develop a novel framework to achieve fine-scale SIC estimation from AMSR2 passive microwave images, including SR network designed for Arctic sea ice and SIC network inspired by the advanced CNN architecture. On the one hand, the SR network in the framework can improve the spatial resolution of original AMSR2 images to reduce the blurring effects from 6.25 to 1.5625 km, providing much sharper sea ice edges and finer texture details, and further reducing the errors of SIC estimation compared with the original AMSR2 data. The following SIC network with the strong regression ability shows good performances for accurately SIC estimation, especially for marginal ice area where thin ice tends to be underestimated or open water area where spurious ice may not be removed cleanly in the ASI algorithm. Experimental results show that the proposed approach is very robust in different regions at different times of the Arctic, and can estimate SIC with rich high-frequency information. Compared with MODIS SIC products at Arctic scale, the proposed model with a RMSE of 5.94% and MAE of 3.04%, outperforms the ASI algorithm using AMSR2 LR data (RMSE = 16.74% and MAE = 7.27%), demonstrating the advantages brought by SR network and SIC network. Future research can explore the potential of the approach in various applications of other sea ice physical parameters and for further improvements.

Acknowledgment

The authors would like to thank JAXA[2] for the provision of AMSR2 brightness temperatures. The MODIS SIC data are provided by University of Bremen.[3]

Author Contribution Statement: Tiantian Feng: Conceptualization, Writing – review and editing, Supervision, Funding acquisition. Rongxing Li: Writing – review and editing. Xiaomin Liu: Investigation, Methodology, Data curation, Writing – original draft.

References

[1] C. Zhang, X. Chen, and S. Ji, "Semantic image segmentation for sea ice parameters recognition using deep convolutional neural networks," *Int. J. Appl. Earth Observ. Geoinformation*, vol. 112, 2022, Art. no. 102885, doi: 10.1016/j.jag.2022.102885.

[2] L. H. Smedsrud, M. H. Halvorsen, J. C. Stroeve, R. Zhang, and K. Kloster, "Fram Strait sea ice export variability and September Arctic sea ice extent over the last 80 years," *Cryosphere*, vol. 11, no. 1, pp. 65–79, Jan. 2017, doi: 10.5194/tc-11-65-2017.

[3] V. Ludwig et al., "The 2018 North Greenland polynya observed by a newly introduced merged optical and passive microwave sea-ice concentration dataset," *Cryosphere*, vol. 13, no. 7, pp. 2051–2073, Feb. 2019, doi: 10.5194/tc-13-2051-2019.

[4] Y. Xian, Z. I. Petrou, Y. Tian, and W. N. Meier, "Super-resolved fine-scale sea ice motion tracking," *IEEE Trans. Geosci. Remote Sens.*, vol. 55, no. 10, pp. 5427–5439, Oct. 2017, doi: 10.1109/TGRS.2017.2699081.

[5] I. de Gelis, A. Colin, and N. Longepe, "Prediction of categorized sea ice concentration from sentinel-1 SAR images based on a fully convolutional network," *IEEE J. Sel. Topics Appl. Earth Observ. Remote Sens.*, vol. 14, pp. 5831–5841, Apr. 2021, doi: 10.1109/JSTARS.2021.3074068.

[6] K. Radhakrishnan, K. A. Scott, and D. A. Clausi, "Sea ice concentration estimation: Using passive microwave and SAR data with a U-Net and curriculum learning," *IEEE J. Sel. Topics Appl. Earth Observ. Remote Sens.*, vol. 14, pp. 5339–5351, Apr. 2021, doi: 10.1109/JSTARS.2021.3076109.

[7] A. Beitsch, L. Kaleschke, and S. Kern, "Investigating high-resolution AMSR2 sea ice concentrations during the February 2013 fracture event in the Beaufort Sea," *Remote Sens.*, vol. 6, no. 5, pp. 3841–3856, Apr. 2014, doi: 10.3390/rs6053841.

[8] S. Marcq and J. Weiss, "Influence of sea ice lead-width distribution on turbulent heat transfer between the ocean and the atmosphere," *Cryosphere*, vol. 6, no. 1, pp. 143–156, 2012, doi: 10.5194/tc-6-143-2012.

[9] Z. I. Petrou, Y. Xian, and Y. Tian, "Towards breaking the spatial resolution barriers: An optical flow and super-resolution approach for sea ice motion estimation," *ISPRS J. Photogrammetry Remote Sens.*, vol. 138, pp. 164–175, 2018, doi: 10.1016/j.isprsjprs.2018.01.020.

[10] A. Bordone Molini, D. Valsesia, G. Fracastoro, and E. Magli, "DeepSUM: Deep neural network for super-resolution of unregistered multitemporal images," *IEEE Trans. Geosci. Remote Sens.*, vol. 58, no. 5, pp. 3644–3656, May 2020 doi: 10.1109/TGRS.2019.2959248.

[11] P. Chakraborty, A. Misra, T. Misra, and S. S. Rana, "Brightness temperature reconstruction using BGI," *IEEE Trans. Geosci. Remote Sens.*, vol. 46, no. 6, pp. 1768–1773, Jun. 2008, doi: 10.1109/TGRS.2008.916082.

[2] [Online]. Available: https://global.jaxa.jp/

[3] [Online]. Available: https://seaice.uni-bremen.de/

[12] D. G. Long and M. J. Brodzik, "Optimum image formation for spaceborne microwave radiometer products," *IEEE Trans. Geosci. Remote Sens.*, vol. 54, no. 5, pp. 2763–2779, May 2016, doi: 10.1109/TGRS.2015.2505677.
[13] T. Hu, F. Zhang, W. Li, W. Hu, and R. Tao, "Microwave radiometer data superresolution using image degradation and residual network," *IEEE Trans. Geosci. Remote Sens.*, vol. 57, no. 11, pp. 8954–8967, Nov. 2019, doi: 10.1109/TGRS.2019.2923886.
[14] X. Liu, T. Feng, X. Shen, and R. Li, "PMDRnet: A progressive multiscale deformable residual network for multi-image super-resolution of AMSR2 Arctic sea ice images," *IEEE Trans. Geosci. Remote Sens.*, vol. 60, pp. 1–18, Feb. 2022, doi: 10.1109/TGRS.2022.3151623.
[15] J. C. Comiso, D. J. Cavalieri, C. L. Parkinson, and P. Gloersen, "Passive microwave algorithms for sea ice concentration: A comparison of two techniques," *Remote Sens. Environ.*, vol. 60, no. 3, pp. 357–384, 1997, doi: 10.1016/S0034-4257(96)00220-9.
[16] J. C. Comiso, *SSM/I ice Concentrations Using the Bootstrap Algorithm*, vol. 1380. Washington, DC, USA: NASA, 1995.
[17] G. Spreen, L. Kaleschke, and G. Heygster, "Sea ice remote sensing using AMSR-E 89-GHz channels," *J. Geophysical Res., Oceans*, vol. 113, no. C2, pp. 1–14, Jan. 2008, doi: 10.1029/2005JC003384.
[18] J. Lu, G. Heygster, and G. Spreen, "Atmospheric correction of sea ice concentration retrieval for 89 ghz AMSR-E observations," *IEEE J. Sel. Topics Appl. Earth Observ. Remote Sens.*, vol. 11, no. 5, pp. 1442–1457, May 2018, doi: 10.1109/JSTARS.2018.2805193.
[19] J. Chi, H. Kim, S. Lee, and M. M. Crawford, "Deep learning based retrieval algorithm for Arctic sea ice concentration from AMSR2 passive microwave and MODIS optical data," *Remote Sens. Environ.*, vol. 231, 2019, Art. no. 111204, doi: 10.1016/j.rse.2019.05.023.
[20] H. Han, S. Lee, H. Kim, and M. Kim, "Retrieval of Summer sea ice concentration in the Pacific Arctic Ocean from AMSR2 observations and numerical weather data using random forest regression," *Remote Sens.-Basel*, vol. 13, no. 12, 2021, Art. no. 2283, doi: 10.3390/rs13122283.
[21] J. Karvonen, "Baltic Sea ice concentration estimation using SENTINEL-1 SAR and AMSR2 microwave radiometer data," *IEEE Trans. Geosci. Remote Sens.*, vol. 55, no. 5, pp. 2871–2883, May 2017, doi: 10.1109/TGRS.2017.2655567.
[22] L. Wang, K. A. Scott, L. Xu, and D. A. Clausi, "Sea ice concentration estimation during melt from dual-pol SAR scenes using deep convolutional neural networks: A case study," *IEEE Trans. Geosci. Remote Sens.*, vol. 54, no. 8, pp. 4524–4533, Aug. 2016, doi: 10.1109/TGRS.2016.2543660.
[23] C. L. V. Cooke and K. A. Scott, "Estimating sea ice concentration from SAR: Training convolutional neural networks with passive microwave data," *IEEE Trans. Geosci. Remote Sens.*, vol. 57, no. 7, pp. 4735–4747, Jul. 2019, doi: 10.1109/TGRS.2019.2892723.
[24] O. Ronneberger, P. Fischer, and T. Brox, "U-net: Convolutional networks for biomedical image segmentation," in *Medical Image Computing and Computer-Assisted Intervention – MICCAI 2015*. New York, NY, USA: Springer, 2015, pp. 234–241.
[25] A. Stokholm, T. Wulf, A. Kucik, R. Saldo, J. Buus-Hinkler, and S. M. Hvidegaard, "AI4SeaIce: Towards solving ambiguous SAR textures in convolutional neural networks for automatic sea ice concentration charting," *IEEE Trans. Geosci. Remote Sens.*, vol. 60, pp. 1–13, Feb. 2022, doi: 10.1109/TGRS.2022.3149323.
[26] D. Malmgren-Hansen et al., "A convolutional neural network architecture for Sentinel-1 and AMSR2 data fusion," *IEEE Trans. Geosci. Remote Sens.*, vol. 59, no. 3, pp. 1890–1902, Mar. 2021, doi: 10.1109/TGRS.2020.3004539.
[27] L. Chen, G. Papandreou, I. Kokkinos, K. Murphy, and A. L. Yuille, "Deeplab: Semantic image segmentation with deep convolutional nets, atrous convolution, and fully connected CRFs," *IEEE Trans. Pattern Anal. Mach. Intell.*, vol. 40, no. 4, pp. 834–848, Apr. 2018.
[28] JAXA, *GCOM-W1 'SHIZUKU' Data Users Handbook*. 2013. [Online]. Available: https://gcom-w1.jaxa.jp/
[29] NSIDC, *Documentation: Polar Stereographic Projection and Grid*. 2016. [Online]. Available: http://nsidc.org/data/polar-stereo/ps_grids.html
[30] L. Chen, Y. Zhu, G. Papandreou, F. Schroff, and H. Adam, "Encoder-decoder with atrous separable convolution for semantic image segmentation," in *Proc. Eur. Conf. Comput. Vis.*, 2018, pp. 801–818.

Tiantian Feng received the B.S. and Ph.D. degrees in photogrammetry and remote sensing from Wuhan University, Wuhan, China, in 2004 and 2010, respectively.

She was a visiting Ph.D. student with the Department of Geography, The State University of New York at Buffalo, Buffalo, NY, USA, from 2007 to 2008. She is currently an Associate Professor with the College of Survey and Geoinformatics, Tongji University, Shanghai, China. Her research interests include multispectral remote sensing image processing, pattern recognition, and remote sensing applications in polar research.

Xiaomin Liu received the B.S. degree in surveying engineering in 2018 from Tongji University, Shanghai, China, where she is currently working toward the Ph.D. degree in surveying and mapping science and technology with the College of Surveying and Geoinformatics (*with a focus on Arctic sea ice monitoring using multisource satellite sensors*).

She is currently involved in the research with the Center for Spatial Information Science and Sustainable Development Applications, Tongji University. Her research interests include passive microwave image processing, deep learning-based super-resolution technology, and Arctic sea ice monitoring using multisource satellite sensors.

Rongxing Li (Senior Member, IEEE) received the B.S. and M.S. (hons.) degrees in surveying and mapping from Tongji University, Shanghai, China, in 1982 and 1984, respectively, and the Ph.D. degree in photogrammetry and remote sensing from the Technical University of Berlin, Berlin, Germany, in 1990.

He was an Associate Professor with the University of Calgary, Calgary, AB, Canada from 1992 to 1996. He was the Lowber B. Strange Professor of Engineering and the Director of the Mapping and GIS Laboratory, Department of Civil, Environmental and Geodetic Engineering, The Ohio State University, Columbus, OH, USA, where he was from 1996 to 2014. Since 2014, he has been a Professor and the Director with the Center for Spatial Information Science and Sustainable Development Applications, Tongji University. His research interests include photogrammetry, digital mapping, polar remote sensing, planetary exploration, and coastal and marine geographic information systems.